and the polyurethane. The urethane segments are hydrophobic and also actively interact with the other hydrophobic materials such as PTFE, and the PMLG segments with the α-helix structure that possess the cytocompatibility. Furthermore, PAU has been firmly coated onto the PTFE fiber and acts as an artificial extracellular matrix. Thus, the radial flow bioreactor system with PTFE non-woven fabric coated with PAU is good for high density and large-scale cell cultured with long-term viability.

In this study, the hepatocytes were isolated from slaughtered porcine, so as to be cultured in the radial flow bioreactor system for HALS. The effectiveness of this system regarding on the activity and maintenance of the hepatocytes functions were examined.

## Materials and Methods

### Isolation of Hepatocytes

By using our method, hepatocytes were isolated from a lobe (about 84 g) of liver of slaughtered adult pig by perfusion technique utilizing dispase and collagenase. The total amount of over $2.6 \times 10^9$ hepatocytes were routinely obtained from a lobe. Hepatocytes of more than 90% viability, determined by trypan blue exclusion method were used for the experiments.

### Perfusion Culture in Radial Flow Bioreactor System

Perfusion culture experiments were performed in a radial flow bioreactor system at 37 °C. The culture medium was composed of WE medium supplemented with 5% (v/v) fetal bovine serum (Sigma, USA), 0.01 μmol/l insulin(Wako Pure Chemical Industries, Ltd., Japan), 0.2 μmol/l dexamethasone (Wako Pure Chemical Industries, Ltd., Japan), 5 μg/l epidermal growth factor (Wako Pure Chemical Industries, Ltd., Japan), $10^5$ U/l penicillin(Sigma, USA), 0.1 g/l streptomycin (Sigma, USA) and 1.5 mmol/l L-ascorbic acid phosphate (Wako Pure Chemical Industries, Ltd., Japan).

Figure 1 shows the schematic diagram of a radial flow bioreactor system. The radial flow bioreactor consists of a PTFE non-woven fabric coated with PAU and hollow fiber. Hepatocytes suspension ($2.0 \times 10^9$ in 50 ml) was inoculated into a medium-preparative tank, and then the medium was perfused to the bioreactor from the medium-preparative tank at a flow rate of 17 ml/min for 10 minutes. Subsequently, the medium was circulated at 84.2 ml/min during the culture experiments. A mixed gas containing air, oxygen and carbon dioxide was introduced into the medium-preparative tank through a control equipment and computer to maintain pH value at 7.3 and diluted oxygen (DO) at 313 μmol/l. The medium exchange was performed every day throughout the culture period.

### Measurement of Hepatocytes Functions

#### *Ammonium Metabolism Rate and Albumin Secretion Rate*

To assess the ammonium metabolism of the cultured hepatocytes, 1 mmol/l $NH_4Cl$ was supplemented into the medium after the medium exchange. Ammonium concentration was measured at 0, 3, and 6 hours after ammonium-loading using a commercially available kit (AMICHEK™ meter; Arkray Factory Inc., Japan). The medium sample was taken before and after the exchange of medium for albumin secretion measure. Albumin secretion was measured by enzyme-linked immunoabsorbant assay, (ELISA).

#### *Glucose Consumption Rate and Oxygen Consumption Rate*

The glucose level was analyzed with a commercially available assay kit (glucose C2 test Wako Pure Chemical Industries, Ltd., Japan). The oxygen uptake rate was estimated by measuring DO at the inlet (medium-conditional vessel, Figure 1 (7)) and the outlet (between 10 and 11 in Figure 1) of the cell adhesive radial flow bioreactor. Measured DO data was recorded by the computer (5, in Figure 1).

 

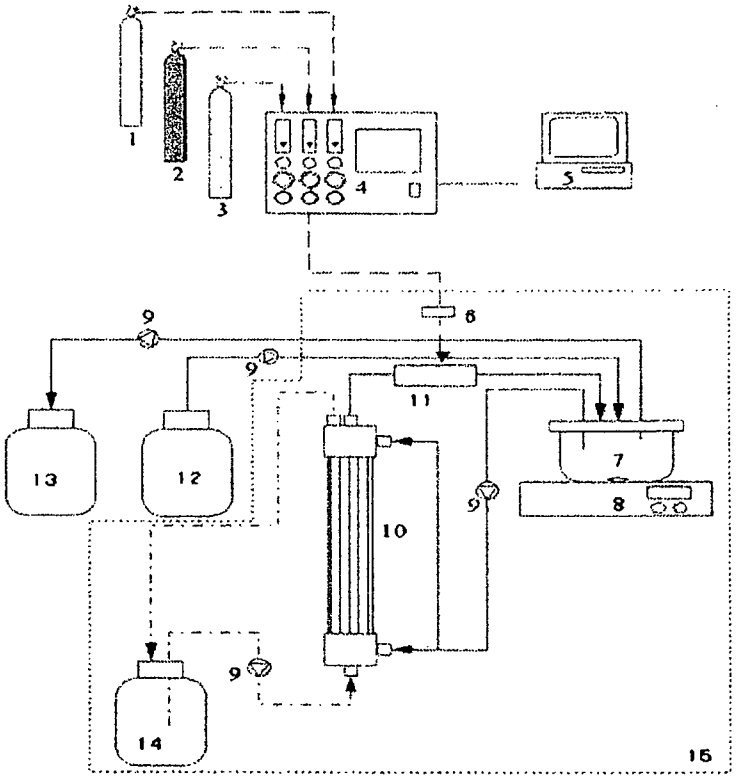


*Figure 1.*
A schematic diagram of radial flow bioreactor for artificial liver assists system.(1) $CO_2$ bomb (2) $O_2$ bomb (3) Air bomb (4) Control equipment (5) Computer (6) Membrane-filter (7) Conditioning vessel (8) Stirrer (9) Peristaltic pump (10) Radial flow bioreactor module (11) Silicone module (12) Fresh medium tank (13) Spent medium tank (14) Plasma bottle (15) Incubator.

### Scanning Electron Micrograph (SEM)

Hepatocytes attached on the culture PAU coated PTFE were fixed with 2.5% glutaraldehyde, and dehydrated with graded ethanol (50, 60, 70, 80, 90, 95 and 99.5%). The specimens after critical point drying with carbon dioxide (Drier EMITECH K-850; Meiwa Shoji Co., Ltd., Japan) were coated with palladium by sputtering (plasma multi coater PMC-5000, Meiwa Shoji Co., Ltd., Japan) and then were subjected to SEM observation (SM-300, Topcon Co., Japan).

### Histological Study

After electrophysiological study, the transverse section (2 μm thick) from scaffold was taken. The section was stained with hematoxylin & eosin (H&E) staining, as well as azan staining to demonstrate esophageal carcinoma tissue group and was examined by light microscopy (DMR, Leica Co., Japan).

## Results

### Ammonium Metabolism Rate and Albumin Secretion Rate

The ammonium metabolizing activity and secreting albumin activity of the hepatocytes were established after being kept for one week at the high value in the bioreactor system as shown in Figure 2 and Figure 3.

The hepatocyte functions showed stable ammonium metabolic rate 75.8 μmol/reactor/h to 132.4 μmol/reactor/h and stable albumin secretion rate; 8.6~24.3 mg/reactor/h after 1 week.

### Glucose Consumption Rate and Oxygen Consumption Rate

The glucose consumption rate has been increasing from 0.16 g/reactor/day to 0.73 g/

 

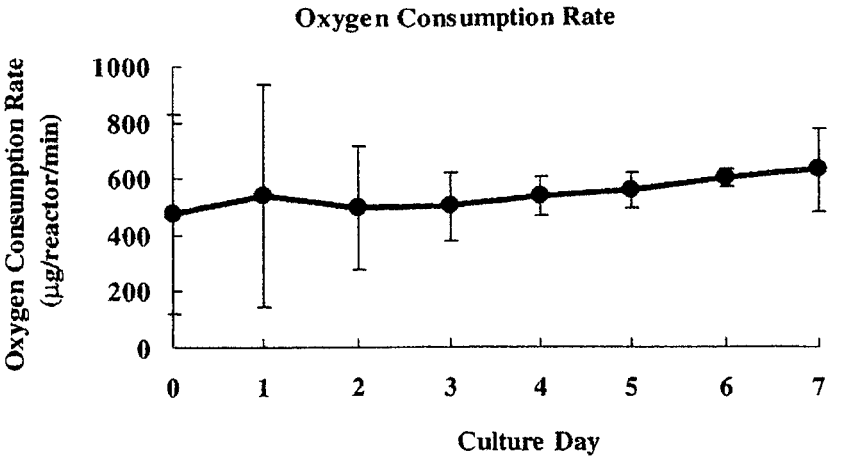


*Figure 5.*
Mean oxygen consumption rate of the hepatocytes cultured in radial flow bioreactor for 7 days.

### SEM and Histological Observation

Figure 6 shows the SEM observation of PTFE non-woven fabric homogeneously coated with PAU before the perfusion culture experiment. The porous structure of PTFE non-woven fabric is maintained and the fabric is changed into hydrophilic and cell adhesive one. Figure 7 shows the SEM observation of the hepatocytes cultured in the radial flow bioreactor after 7 days of culture experiment. Large amount of hepatocytes were aggregated, and adhered onto the surface of PTFE coated with PAU. In addition, the hepatocytes were covered with extracellular matrix (ECM)-like layer. These were proven by H&E and Azan staining as shown in Figure 8. H&E staining pictures show many hepatocyte cells. Azan staining pictures show the existence of connective tissue including collagen.

## Discussion

In this study, the activities of ammonia metabolism of hepatocytes were significantly 200 times higher than that of hepatocytes cultured in radial flow bioreactor consists of porous glass bead microcarriers that we have conducted earlier

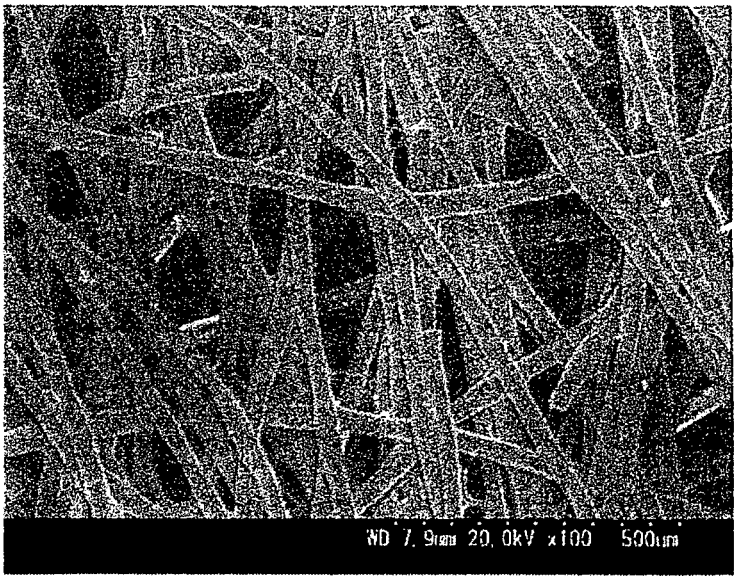


*Figure 6.*
SEM micrograph of PTFE coated with PAU (×100).

 

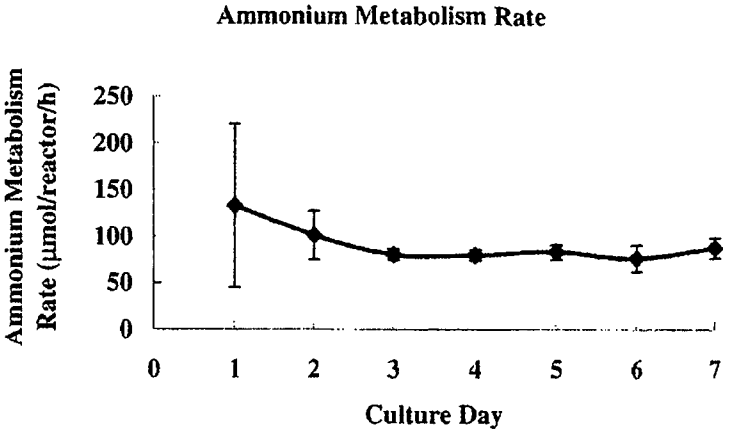


*Figure 2.*
Mean ammonium metabolic rate of the hepatocytes cultured in radial flow for 7 days.

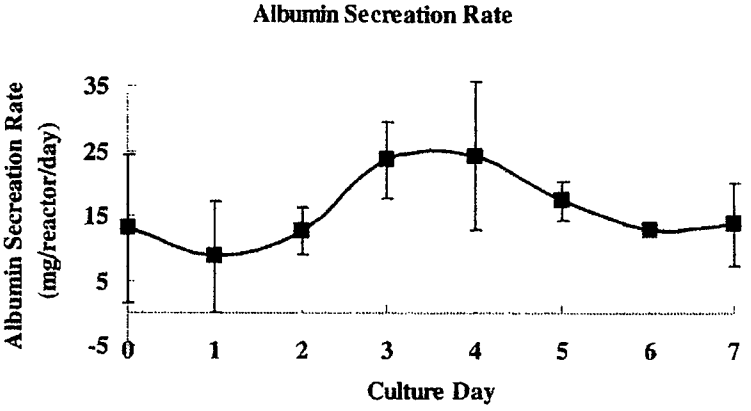


*Figure 3.*
Mean albumin secretion rate of the hepatocytes cultured in radial flow bioreactor for 7 days.

reactor/day as shown in Figure 4, whilst the oxygen consumption rate has also been increasing from 475 μg/reactor/min to 630 μg/reactor/min as shown in Figure 5. These results indicate that hepatocytes proliferate properly with the increasing of respiration rate and energy produced during 7 days culture.

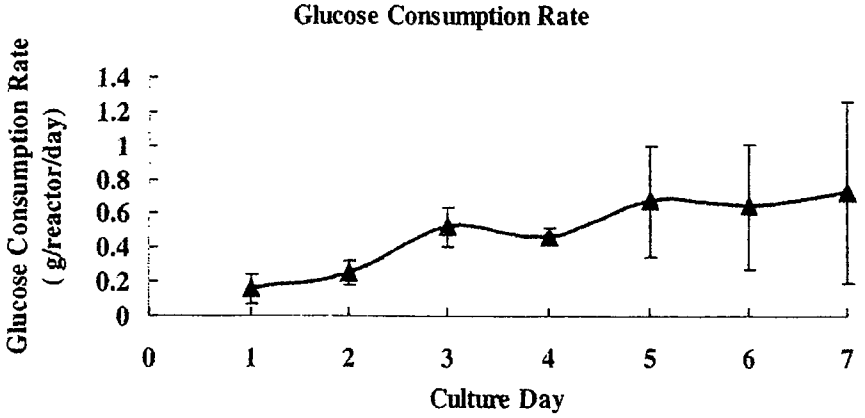


*Figure 4.*
Mean glucose consumption rate of the hepatocytes cultured in radial flow bioreactor for 7 days.

 

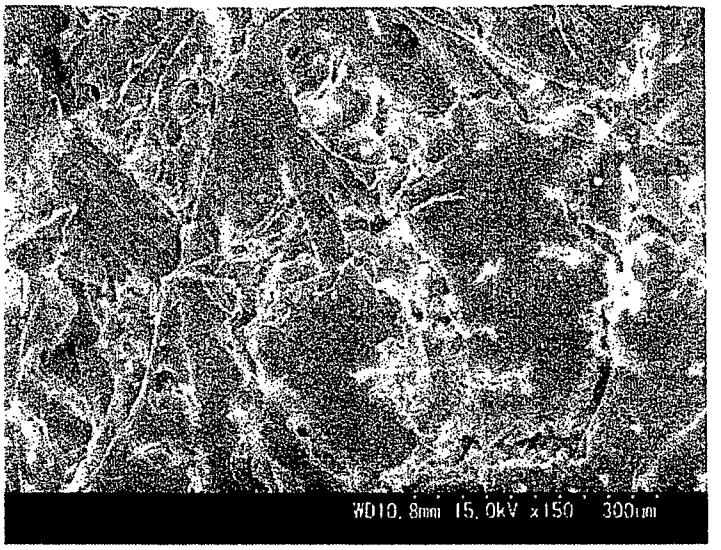


(a) (x150)

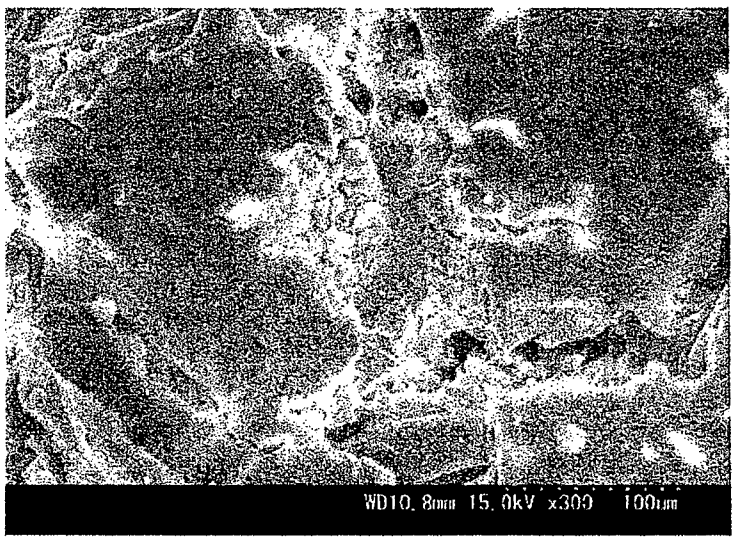


(b) (x300)

***Figure 7.***
SEM micrograph of cultured in radial flow bioreactor. (a) (×150), (b) (×300).

(data not shown). This result suggests that by enhancing the immobilized hepatocytes on the PTFE non-woven fabric coated with PAU may also enhances the functional activities of hepatocytes as shown in Figure 2 and Figure 3. Uchida et al.[27,28] had demonstrated that coating with PAU hydrophobic PTFE been changed to hydrophilic PTFE but still maintaining the porous structure. PAU consists of the block copolymer segments of urethane, with a small amount of PMLG at the center of the copolymer chain, where most of the PMLG accumulate at both terminals of the copolymer chain. The urethane segments have good adhesion to other materials, and the PMLG segments have the α-helix structure of protein which posses the high cytocompatibility as shown in Figure 7 and 8.

HALS needs sufficient oxygen supply, which is so different from other artificial organs.[10–19] To overcome this problem, radial flow with porous hepatocytes-immobilizing is effective for HALS.[20–26] From this study, radial flow of medium supply and PAU coated PTFE non-woven fabric scaffold is a good combination for HALS as shown in Figure 4 and Figure 5. The oxygen consumption as well as the glucose consumption rate increased and the hepatocytes were covered with ECM, look-like nature liver tissue even after 7 days

 

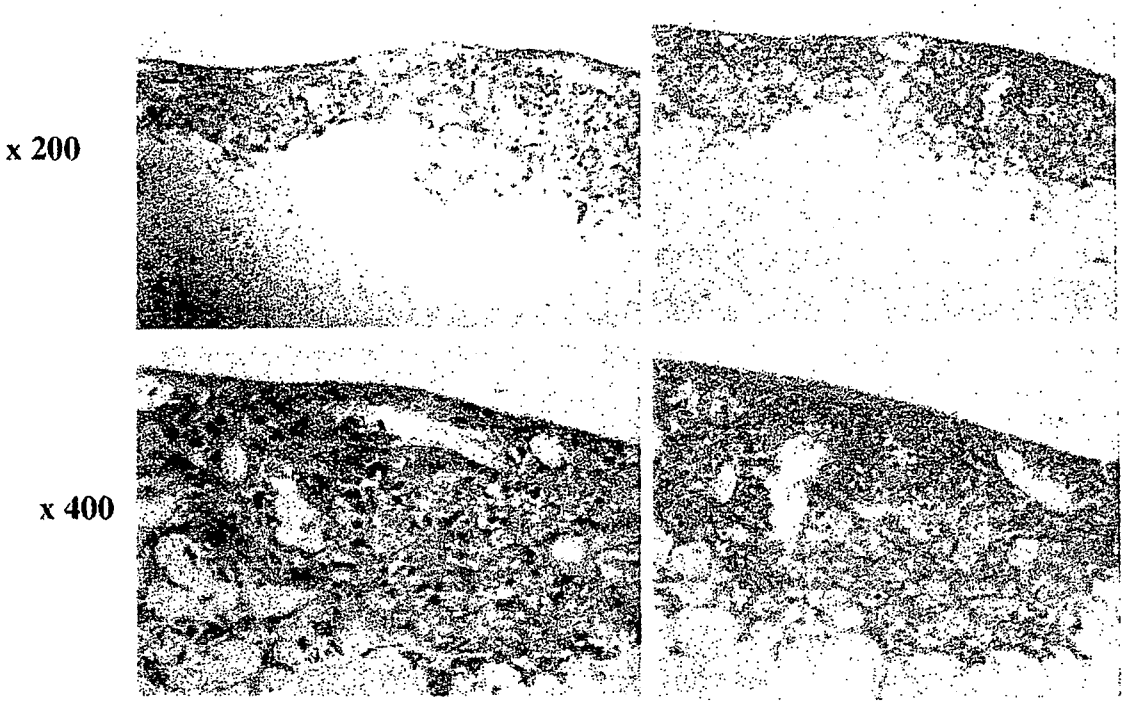


***Figure 8.***
H&E staining and azan staining of cultured in radial flow bioreactor.

cultured in this projected bioreactor. However, we need to do pre-clinical experiment on animal before any clinical use.

*Acknowledgements:* We thank Ms Sachiyo Fujinobu for outstanding technical assistant and to Tun Hussein Onn Collage University of Technology Malaysia for funding Mr. Azizi Miskon for his Masters and PhD at Kyushu Institute of Technology and Osaka University.

[1] T. Hui, J. Rozga, A. A. Demetriou, Bioartificial liver support. *J. Hepatobiliary Pancreat. Surg.* **2001**, *8*, 1–15.
[2] J. Rozga, M. D. Holzman, M. S. Ro, D. W. Griffin, D. F. Neuzil, T. Gloegio, A. D. Moscioni, A. A. Demetriou, Development of a hybrid bioartificial liver. *Ann. Surg.* **1993**, *217*, 509–511.
[3] K. Naruse, Y. Sakai, I. Nagashima, G. X. Jiang, M. Suzuki, T. Muto, Development of a new bioartificial liver module filled with porcine hepaocyte immobilized on non-woven fabric. *Int. J. Artificial Organs* **1996**, *19*, 347–352.
[4] K. Naruse, Y. Sakai, I. Nagashima, G. X. Jiang, M. Suzuki, T. Muto, Comparison of porcine hepatocyte spheroids and single hepatocytes in the non-woven fabric bioartificial liver module. *Int. J. Artif. Organ* **1996**, *19*, 605–609.
[5] T. Kimura, H. Kurosawa, M. Nishizawa, Y. Omura, N. Tokunaga, Y. Ogata, Y. Amano, A novel polyurethane membrane enables a bioartificial liver with a fixed-bed to immobilize hepatocytes at high cell density. *Jpn. J. Artif. Organs* **1999**, *28*, 475–479 (in Japanese).
[6] T. Sajiki, H. Iwata, H. J. Paek, T. Tosha, S. Fujita, Y. Ueda, Y. G. Park, B. Zhu, S. Satoh, I. Ikai, Y. Yamaoka, Y. Ikada, Morphologic studies of hepatocytes entrapped in hollow fibers of a bioartificial liver. *ASAIOJ* **2000**, *46*, 49–5.
[7] J. Rozga, L. Podesta, E. Lepage, A. D. Morsiani, A. Hoffman, L. Sher, F. Villamil, G. Woolf, M. Megrath, L. Kong, H. Rosen, T. Lanman, J. Vierling, L. Makokawa, A. A. Demitrou, A bioartificial liver to treat fulminant hepatic failure. *Ann. Surg.* **1994**, *219*, 538–546.
[8] N. L. Sussman, G. T. Gislason, C. A. Conlin, J. H. Kelly, The hepatix extracorporeal liver assist device: initial clinical experience. *Artif. Organs* **1994**, *18*, 390–396.
[9] A. J. Ellis, R. D. Hughes, J. A. Wendon, J. Dunne, P. G. Langley, J. H. Kelly, G. T. Gislason, N. L. Sussman, R. Williams, Pilot-controlled trial of the extracorporeal liver assist device in acute liver. *Hepatology* **1996**, *24*, 1446–1451.
[10] A. Rotem, M. Toner, S. Bhatia, B. D. Foy, R. G. Tompkins, M. L. Yarmush, Oxygen is a factor determining in vitro tissue assembly: effects on attachment and spreading of hepatocytes. *Biotechnol. Bioeng.* **1994**, *43*, 654–660.
[11] B. D. Foy, J. Lee, J. Morgan, M. Toner, R. G. Tompkins, M. L. Yarmush, Optimization of hepatocyte attachment to microcarriers: importance of oxygen. *Biotechnology Bioeng.* **1993**, *42*, 579–588.

 

[12] G. A. Ledezma, A. Folch, S. N. Bhatia, U. J. Balis, M. L. Yarmush, M. Toner, Numerical model of fluid flow and oxygen transport in a radial-flow microchannel containing hepatocytes. *J. Biomech. Eng.* **1999**, *121*(1), 58–64.

[13] P. D. Hay, A. R. Veitch, J. D. Gaylor, Oxygen transfer in a convection-enhanced hollow fiber bioartificial liver. *Artif. Organs* **2001**, *25*(2), 119–130.

[14] M. Nishikawa, J. Uchio, M. Matsushita, M. Takahashi, K. Taguchi, M. Koike, H. Kamachi, H. Kon, Optimal oxygen tension conditions for functioning cultured hepatocytes in vitro. *Artif. Organs* **1996**, *20*(2), 169–177.

[15] A. W. Tiles, H. Baskaran, P. Roy, M. L. Yarmush, M. Toner, Effects of oxygenation and flow on the viability and function of rat hepatocytes cocultured in a microchannel flate-pate bioreactor. *Biotechnol. Bioeng.* **2001**, *73*(5), 379–89.

[16] P. D. Hay, A. R. Veitch, J. D. Gaylor, Oxygen transfer in a convection-enhanced hollow fiber bioartificial liver. *Artif. Organs* **2001**, *25*(2), 119–130.

[17] K. Yanagi, N. Ohsima, Improvement of metabolic performance of cultured hepatocytes by high oxygen tension in the atmosphere. *Artif. Organs* **2001**, *25*(1), 1525–1594.

[18] I. Jasmund, A. Langsch, R. Simmoteit, A. Bader, Cultivation of primary porcine hepatocytes in an OXY-HFB for use as a bioartificial liver device. *Biotechnol. Prog.* **2002**, *18*(4), 839–846.

[19] R. E. McClelland, J. M. MacDonald, R. N. Coger, Modelling $O_2$ transport within engineered hepatic devices. *Biotechnol. Bioeng.* **2003**, *82*(1), 12–27.

[20] J. C. Gerlach, K. Zeilinger, A. Grebe, G. Puhl, G. Pless, I. Sauer, A. Grunwald, N. Schnoy, C. Muller, P. Neuhaus, Recovery of preservation-injured primary human hepatocytes and nonparenchymal cells to tissulike structures in large-scale bioreactors for liver support: an Initial transmission electron microscopy study. *J. Invest. Surg.* **2003**, *16*(2), 83–92.

[21] H. Iwata, Y. Ueda, Pharamacokinetic considerations in development of a bioartificial liver *Clin. Pharmacokinet.*

[22] M. Maruyama, T. Totsugawa, T. Kunieda, T. Okitsu, N. Shibata, M. Takesue, Y. Kurabayashi, M. Oshita, S. Nakaji, M. Kodama, N. Tanaka, N. Kobayashi, Hepatocyte isolation and transplantation in the pig. *Cell Transplant* **2003**, *26*(2), 593–8.

[23] C. Mischiati, A. C. Puviani, M. Brogli, S. Guarniero, A. Sereni, L. Breda, D. Ricci, D. Galavotti, E. Morsiani, R. Gambari, Modulation of pro-apoptotic (Bax) and anti-apoptic(Bcl-2) gene expression in isolated porcine hepatocytes perfused within a radial-flow bioreactor after low-temperature storing. *Int. J. Artif. Organs* **2003**, *26*(2), 139-48.

[24] T. H. Yang, H. Miyoshi, N. Ohshima, Novel cell immobilization method utilizing centrifugal force to achieve high-density hepatocytes culture in porous scaffold. *J. Biomed. Mater. Res.* **2001**, *55*(3), 397–86.

[25] S. Nagamori, S. Hasumura, T. Matsuura, H. Aizaki, M. Kawada, Developments in bioartificial liver research: concepts, performance, and applications. *J. Gastroenterol.* **2003**, *35*, 493–503.

[26] T. H. Yang, H. Miyoshi, N. Ohshima, Novel cell immobilization method utilizing centrifugal force to achieve high-density hepatocytes culture in porous scaffold. *J. Biomed. Mater. Res.* **2001**, *55*(3), 379–386.

[27] S. Uchida et al. New copolymers of amino acid and urethane (PAU) in which a polyurethane is combined with poly(g-methyl-L-glutameate)(PMLG); are synthesized. *J. Polymer Science Part A: Polymer Chemistry* **1999**, *37*, 383–389.

[28] A new vascular prosthetesis coated with polyamino-acid urethane copolymer (PAU) to enhance endothelialization. Wiley Periodicals 2001 10.1002/jbm.10137

 

IOP PUBLISHING PHYSICS IN MEDICINE AND BIOLOGY

Phys. Med. Biol. 52 (2007) 1893–1908 doi:10.1088/0031-9155/52/7/009

# Separation of input function for rapid measurement of quantitative $CMRO_2$ and CBF in a single PET scan with a dual tracer administration method

**Nobuyuki Kudomi, Hiroshi Watabe, Takuya Hayashi and Hidehiro Iida**

Department of Investigative Radiology, Advanced Medical-Engineering Center, National Cardiovascular Center-Research Institute, 5-7-1, Fujishirodai, Suita, Osaka 565-8565, Japan

E-mail: kudomi@ri.ncvc.go.jp

Received 1 September 2006, in final form 3 January 2007
Published 12 March 2007
Online at stacks.iop.org/PMB/52/1893

**Abstract**

Cerebral metabolic rate of oxygen ($CMRO_2$), oxygen extraction fraction (OEF) and cerebral blood flow (CBF) images can be quantified using positron emission tomography (PET) by administrating $^{15}O$-labelled water ($H_2^{15}O$) and oxygen ($^{15}O_2$). Conventionally, those images are measured with separate scans for three tracers $C^{15}O$ for CBV, $H_2^{15}O$ for CBF and $^{15}O_2$ for $CMRO_2$, and there are additional waiting times between the scans in order to minimize the influence of the radioactivity from the previous tracers, which results in a relatively long study period. We have proposed a dual tracer autoradiographic (DARG) approach (Kudomi *et al* 2005), which enabled us to measure CBF, OEF and $CMRO_2$ rapidly by sequentially administrating $H_2^{15}O$ and $^{15}O_2$ within a short time. Because quantitative CBF and $CMRO_2$ values are sensitive to arterial input function, it is necessary to obtain accurate input function and a drawback of this approach is to require separation of the measured arterial blood time–activity curve (TAC) into pure water and oxygen input functions under the existence of residual radioactivity from the first injected tracer. For this separation, frequent manual sampling was required. The present paper describes two calculation methods: namely a linear and a model-based method, to separate the measured arterial TAC into its water and oxygen components. In order to validate these methods, we first generated a blood TAC for the DARG approach by combining the water and oxygen input functions obtained in a series of PET studies on normal human subjects. The combined data were then separated into water and oxygen components by the present methods. CBF and $CMRO_2$ were calculated using those separated input functions and tissue TAC. The quantitative accuracy in the CBF and $CMRO_2$ values by the DARG approach did not exceed the acceptable range, i.e., errors in those values were within 5%, when the area under the curve in the input function of the second tracer was larger than half of the first one. Bias and deviation in those values were also compatible to that of the conventional method, when noise

0031-9155/07/071893+16$30.00  

was imposed on the arterial TAC. We concluded that the present calculation based methods could be of use for quantitatively calculating CBF and $CMRO_2$ with the DARG approach.

## 1. Introduction

Cerebral metabolic rate of oxygen ($CMRO_2$), oxygen extraction fraction (OEF) and cerebral blood flow (CBF) images have enabled us to understand the pathophysiological basis of cerebrovascular disorders. Positron emission tomography (PET) allows us to quantitatively measure the CBF and $CMRO_2$. These measurements can be achieved using a protocol involving separate PET scans, one after the administration of each of three distinct $^{15}O$-labelled radioactive tracers: $H_2{}^{15}O$ or $C^{15}O_2$ for CBF, $^{15}O_2$ for $CMRO_2$, and $C^{15}O$ for cerebral blood volume (CBV) (Frackowiack *et al* 1980a, 1980b, Mintun *et al* 1984, Lammertsma and Jones 1983). However, the complex procedure and its relatively long protocol often limit its applicability and also make it difficult to perform at different physiological conditions.

Quantitative images of CBF and $CMRO_2$ by PET are calculated on the basis of a single-tissue compartment model of oxygen and water kinetics (Frackowiack *et al* 1980a, 1980b, Mintun *et al* 1984, Lammertsma and Jones 1983). The steady-state method (Subramanyam *et al* 1978, Lammertsma *et al* 1982, Correia *et al* 1985, Okazawa *et al* 2001a, 2001b) has been employed in a number of studies in which quantitative images are estimated from data acquired while in the steady state reached during continuous inhalation of $C^{15}O_2$ and $^{15}O_2$. This method can be employed using a simple procedure and mathematical formula, but has several limitations. A prolonged data-acquisition period (approximately 1 h) is required, and the procedure is sensitive to error sources such as statistical noise and tissue heterogeneity (Lammertsma *et al* 1982, Correia *et al* 1985). An additional drawback is the relatively high level of radiation exposure required to reach the steady state.

An alternative autoradiographic method (ARG) using only short administration times for each of the three tracers, i.e., the three-step autoradiographic method (3SARG) has been developed (Mintun *et al* 1984) and subsequently simplified and optimized (Iida *et al* 1993, Sadato *et al* 1993, Hatazawa *et al* 1995, Shidahara *et al* 2002, Hattori *et al* 2004). CBF images can be obtained by a $H_2{}^{15}O$ autoradiographic method, using a PET counts-versus-CBF nomogram, which follows a simple look-up table procedure (Raichle *et al* 1983, Herscovich *et al* 1983, Kanno *et al* 1987); the quantitative accuracy of these images is improved when influence of input delay, which is the time difference between brain input function and detector device, and dispersion, which is caused by flow speed difference of liquid in a catheter tube due to viscosity, are corrected (Iida *et al* 1986, 1988). $CMRO_2$ and the oxygen extraction fraction (OEF) can be estimated using data acquired during $^{15}O_2$ inhalation, but must be corrected for clearance of radioactivity associated with CBF (Mintun *et al* 1984), CBV and the level of recirculating radioactive water (Iida *et al* 1993). Although the total time required for 3SARG is less than that of the steady-state method, it still requires at least half an hour, with waiting times between the scans to reduce the radioactivity of the tracer administered previously.

There have been other attempts to obtain CBF and $CMRO_2$ images more rapidly (Huang *et al* 1986, Holden *et al* 1988, Meyer *et al* 1987, Ohta *et al* 1992, Ho and Feng 1999). Mathematical refinement has allowed images to be generated from data from a single scan alone upon a bolus inhalation of $^{15}O_2$. The quality of the image suffers, however, from statistical noise due to the lack of predictability of the multiple parameters of CBF, $CMRO_2$, and the arterial vascular compartment ($V_0$) and the limited acquisition time (Meyer *et al* 1987, Ohta *et al* 1992). Therefore, this technique has not been generally applied in clinical settings,

but has been used primarily for research purposes (Fujita *et al* 1999, Vafaee and Gjedde 2000, Okazawa *et al* 2001a, 2001b, Mintun *et al* 2002).

Recently, rapid CBF and $CMRO_2$ measurement was achieved by administration of dual tracers during a single PET scan and the use of an integration method, i.e., dual tracer autoradiographic (DARG) approach (Kudomi *et al* 2005). This approach can shorten the total study period for both CBF and $CMRO_2$ measurement as compared to the 3SARG approach. It is thus expected to serve as a tool for faster or repeated assessment of flow and metabolism during multiple physiological or pathological conditions while maintaining the image quality and quantitative accuracy.

The DARG protocol was typically implemented in a short time interval of 3 min in a single PET scan conducted during the sequential administration of $H_2^{15}O$ and $^{15}O_2$. A mathematical formula based on the integration method was derived to calculate the values of CBF, OEF and $CMRO_2$ from the PET scan data, and was applicable to the data obtained after the administration of tracers in either order, i.e. $H_2^{15}O$ injection followed by $^{15}O_2$ inhalation ($H_2^{15}O$–$^{15}O_2$) or $^{15}O_2$ inhalation followed by $H_2^{15}O$ injection ($^{15}O_2$–$H_2^{15}O$). In the formula, the radioactivity concentrations in the artery, i.e. arterial input functions for the $^{15}O$-labelled oxygen and $^{15}O$-labelled water must be provided in order to compute the quantitative CBF and $CMRO_2$ values.

The arterial input function of whole blood including oxygen and water is usually obtained from a continuously measured arterial blood time–activity curve (TAC) by a beta-ray detector (Kanno *et al* 1987, Iida *et al* 1986) or coincidence detector (Eriksson *et al* 1988, Eriksson and Kanno 1991, Votaw *et al* 1998, Kudomi *et al* 2003). In the DARG approach, it is necessary to separate the $^{15}O_2$ and $H_2^{15}O$ contents in the arterial TAC during the second phase of the scan because the arterial blood contains not only the radioactivity of the second tracer but also the residual activity of the first tracer. Thus, the radioactivity in the arterial blood during the second phase of the scan is always the summation of the radioactivity from $^{15}O_2$ and $H_2^{15}O$. Moreover, after its administration, $^{15}O_2$ coexists in arterial blood with labelled or recirculating $H_2^{15}O$, which is a metabolite. A modelling approach (Iida *et al* 1993) enables us to predict the TAC of the recirculating water, but this approach is based on an assumption that there is no radioactivity in the arterial blood at the time of $^{15}O_2$ administration and it cannot be applied when residual radioactivity of $H_2^{15}O$ exists in the arterial blood. Instead of using the modelling approach, Kudomi *et al* (2005) performed frequent manual sampling of arterial blood and centrifugation to separate plasma from whole blood in order to predict the recirculating water content in the whole blood. However, this procedure is labour intensive and hampers the clinical application of the DARG protocol.

In this paper, we have proposed two methods: (A) a linear method and (B) a model-based method to separate the $^{15}O_2$ and $H_2^{15}O$ contents from a measured arterial TAC in which both $^{15}O_2$ and $H_2^{15}O$ coexisted for the DARG approach. By these methods, no manual sampling of arterial blood is required to separate the $^{15}O_2$ and $H_2^{15}O$ contents. In order to evaluate the proposed methods, simulation studies were performed.

## 2. Materials and methods

### *2.1. Separation methods*

In this section, we described two separation methods. In both methods, the separation procedure from measured whole blood TAC ($A_t(t)$) to input functions of pure $H_2^{15}O$ ($F_w(t)$) and $^{15}O_2$ ($F_o(t)$) consists of two parts, one is to account for residual activity for the first tracer

during the second phase, and the other is to account for the metabolic product of $^{15}O_2$, i.e., recirculating water.

*(A) Linear method.* For the $H_2^{15}O$–$^{15}O_2$ protocol, we first estimated the TAC for the residual radioactivity from the first tracer ($H_2^{15}O$) remaining during the second phase by extrapolating the combined TAC in the first phase by the following linear function:

$$F_L(t) = at + b \tag{1}$$

where $t$ is the time and $a$ and $b$ are the parameters being estimated. We then subtracted the fitting function equation (1) from the measured TAC in the second phase, and obtained first ($F_1(t)$) and second tracer TAC ($F_2(t)$) as

$$\begin{aligned} F_1 &= A_t(t) \quad (t < t_{2nd}) \\ &= F_L(t) \quad (t > t_{2nd}) \end{aligned} \tag{2}$$

$$\begin{aligned} F_2 &= 0 \ (t < t_{2nd}) \\ &= A_t(t) - F_L(t) \quad (t > t_{2nd}) \end{aligned} \tag{3}$$

where $t_{2nd}$ is the time of second tracer administration. Second, the TAC of the metabolic product (recirculating water) ($F_{rw}(t)$) following $^{15}O_2$ administration was estimated in the second phase, using the modelling approach described previously (Iida *et al* 1993). The model proposed the assumption of a fixed rate constant ($k = 0.0722$ min$^{-1}$) for production of recirculating water, and predicted the appearance of the recirculating water from the measured whole blood TAC as

$$F_{rw}(t) = kF_2(t - \Delta t) \otimes e^{-kt} \tag{4}$$

where $\Delta t$ indicates the delay time of appearance of recirculating water and $\otimes$ denotes the convolution integral. Finally, the TAC of the recirculating water (equation (4)) was added to $F_1(t)$ to obtain a TAC for $H_2^{15}O$ ($F_w(t)$), and also subtracted from $F_2(t)$ to obtain a pure TAC for $^{15}O_2$ ($F_o(t)$), i.e.,

$$\begin{aligned} F_w &= A_t(t) \quad (t < t_{2nd}) \\ &= F_L(t) + F_{rw}(t) \quad (t > t_{2nd}) \end{aligned} \tag{5}$$

$$\begin{aligned} F_o &= 0 \ (t < t_{2nd}) \\ &= A_t(t) - F_L(t) - F_{rw}(t) \quad (t > t_{2nd}). \end{aligned} \tag{6}$$

For the $^{15}O_2$–$H_2^{15}O$ protocol, we first obtained the TAC for the recirculating water due to the metabolism of oxygen during the first phase of $^{15}O_2$ administration using the modelling approach (Iida *et al* 1993) as

$$F_{rw}(t) = kA_t(t - \Delta t) \otimes e^{-kt} \quad (t < t_{2nd}) \tag{7}$$

and then separated the whole blood TAC into pure TACs for $^{15}O_2$ and $H_2^{15}O$ during the first phase. Second, we estimated the TAC for the residual radioactivity of $^{15}O_2$ during the second phase by extrapolating the estimated arterial $^{15}O_2$ TAC from the first phase by a linear function as in the case of the $H_2^{15}O$–$^{15}O_2$ protocol and then obtained pure TAC for $H_2^{15}O$ and $^{15}O_2$, i.e.,

$$\begin{aligned} F_w &= F_{rw}(t) \quad (t < t_{2nd}) \\ &= A_t(t) - F_L(t) \quad (t > t_{2nd}) \end{aligned} \tag{8}$$

$$\begin{aligned} F_o &= A_t(t) - F_{rw}(t) \quad (t < t_{2nd}) \\ &= F_L(t) \quad (t > t_{2nd}) \end{aligned} \tag{9}$$

where if $F_L(t)$ was less than 0, its value was set to zero.

*(B) Model-based method.* The input function after the injection of $H_2^{15}O$ was assumed to be the sum of two exponentials that were convolved with a Gauss function:

$$F'_w(t) = w_1 \exp(-w_3 t) \otimes g(w_5 t) + w_2 \exp(-w_4 t) \otimes g(w_6 t) \tag{10}$$

where $F'_w$ represents the blood TAC for water administration but does not include the recirculating water from $^{15}O_2$ administration and $g(x)$ is a Gauss function as

$$g(px) = \exp(-p^2 x^2) \tag{11}$$

$w_i$ ($i = 1$–6) are the parameters estimated.

The administration of $^{15}O_2$ is usually performed by the continuous inhalation of $^{15}O_2$ gas. The input function after the inhalation of $^{15}O_2$ was modelled using a rectangular function ($f_{rect}$) as follows:

$$F'_o(t) = f_{rect}(t) \otimes [o_1 \exp(-o_3 t) \otimes g(o_5 t) + o_2 \exp(-o_4 t) \otimes g(o_6 t)] \tag{12}$$

where $F'_o$ represents the sum of the TAC of pure $^{15}O_2$ and recirculating water, and $o_i$ ($i = 1$–6) are the parameters to be estimated. $f_{rect}$ is defined as

$$\begin{aligned} f_{rect}(t) &= \text{constant} \quad (T_1 < t < T_2) \\ f_{rect}(t) &= 0 \qquad\quad (t < T_1 \text{ or } t > T_2) \end{aligned} \tag{13}$$

where $T_1 < t < T_2$ corresponds to the period of tracer administration.

The model function for the combined input function ($F_t$), i.e., whole blood TAC, is expressed by summing $F'_w(t)$ (equation (10)) and $F'_o(t)$ (equation (12)) as follows:

$$F_t(t) = F'_w(t - T_w) + F'_o(t - T_o) \tag{14}$$

where $T_w$ and $T_o$ denote the start time of $H_2^{15}O$ and $^{15}O_2$ administration, respectively. In our PET study, the interval between the injections of the two tracers was 180 s; therefore $T_w = 0$ and $T_o = 180$ s for the $H_2^{15}O$–$^{15}O_2$ protocol and $T_w = 180$ and $T_o = 0$ s for the $^{15}O_2$–$H_2^{15}O$ protocol.

The measured blood TAC was fitted for the whole period using the model function $F_t(t)$ in equation (14) by the variable-metric method (pseudo-Gauss–Newton method), and $F'_w$ and $F'_o$ were then obtained as the separated input functions. All computations, including the fitting operation, were carried out in the PAW environment (http://wwwasd.web.cern.ch/wwwasd/paw/). Finally, the TAC for recirculating water was obtained by applying the modelling approach (Iida *et al* 1993) using the obtained $F'_o(t)$ as

$$F_{rw}(t) = k F'_o(t - \Delta t) \otimes e^{-kt} \tag{15}$$

and the estimated recirculating water TAC was added to $F'_w(t)$ and subtracted from the obtained $F'_o(t)$, which resulted in the pure TACs of $H_2^{15}O$ and $^{15}O_2$, i.e.,

$$\begin{aligned} F_w(t) &= F'_w(t) + F_{rw}(t) \\ F_o(t) &= F'_o(t) - F_{rw}(t). \end{aligned} \tag{16}$$

### 2.2. *Simulation studies*

The reliability of the present methods was tested using actual blood TACs obtained in a series of PET studies.

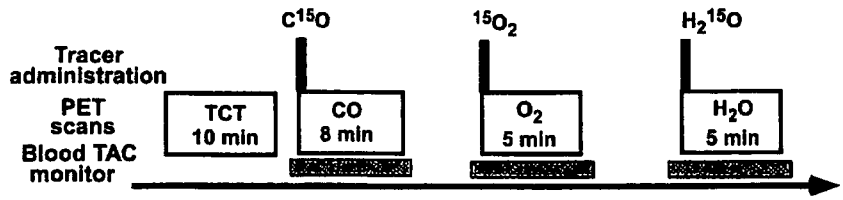


**Figure 1.** PET study protocol on normal human subjects. After a 10 min transmission scan and $C^{15}O$ (3000 MBq) emission scan, gaseous $^{15}O_2$ (3000 MBq) was inhaled for 1 min and a scan for 5 min was started at the same time. After sufficient time for radioactive decay of $^{15}O_2$, a $H_2^{15}O$ PET scan for 5 min was started with an intravenous administration of $H_2^{15}O$ (1110 MBq). The concentration of the radioactivity in the arterial blood was monitored (blood TAC monitor) continuously by a beta-ray detector, started at 30 s before and stopped at 30 s after the PET scan.

*2.2.1. PET studies.* A series of PET scans to measure the CBF and $CMRO_2$ were carried out on ten normal human subjects. All subjects were males ($n = 10$, age = 24.6 ± 3.3 years, body weight = 65.6 ± 9.0 kg), who provided written informed consent. The PET procedures were approved by the ethical committee of the National Cardiovascular Center. The details of the PET procedure have been described previously (Shidahara *et al* 2002). The PET scanner used was an ECAT EXACT 47 (CTI Inc., Knoxville, USA). After a 10 min transmission scan and emission scan with the administration of 3000 MBq of $C^{15}O$ for 8 min, gaseous $^{15}O_2$ of 3000 MBq was inhaled for 1 min, and a dynamic scan for 5 min was started at the same time as the inhalation. After allowing sufficient time for radioactive decay of $^{15}O_2$, another scan for 5 min was initiated with an intravenous administration of $H_2^{15}O$ into the right brachial vein. The dose was approximately 1110 MBq and the infusion period was 10 s. The study protocol is shown in figure 1.

The concentration of the radioactivity in the arterial blood was monitored continuously by means of a beta-ray detector (Kanno *et al* 1987, Iida *et al* 1986) during the PET scan. A catheter was inserted into the brachial artery, and blood was withdrawn at a flow rate of 4 ml $min^{-1}$. The inner diameter of the tube was approximately 1.3 mm, and the distance from the catheter to the detector was 20–25 cm. Continuous blood sampling was started at 30 s before the start of the PET scan and stopped at 30 s after the end of the scan. For each PET study, the beta-ray detector was calibrated against a NaI(Tl) well counter which was cross calibrated to the PET scanner. The calibration was carried out using $H_2^{15}O$ filled in the tube. The cross calibration factor of the detector against the well counter was from 50 to 100 cps $g^{-1}$ $cps^{-1}$.

*2.2.2. Simulated input function for DARG protocol and separation.* Combined input function (CIF) as a simulated input function was generated by combining the experimentally obtained input functions for $H_2^{15}O$ and $^{15}O_2$ administration. Ten sets of $H_2^{15}O$ and $^{15}O_2$ arterial TACs obtained in the series of PET studies were used to generate the CIF.

It is known that the measured arterial TAC is more dispersed and delayed relative to the true input TAC in the brain, due to transverses of blood in peripheral artery and catheter tube before reaching the detector (Iida *et al* 1986, 1988, 1989, 2000, Lammertsma *et al* 1990), those terms in blood TAC were corrected. Dispersion correction (Iida *et al* 1986) was applied to the arterial blood TACs with $H_2^{15}O$ and $^{15}O_2$. Also, delay was corrected for the $H_2^{15}O$ arterial TAC (Iida *et al* 1988, Shidahara *et al* 2002) and that for $^{15}O_2$ administration was corrected by applying the same time as for $H_2^{15}O$ for the same subject. For the arterial blood TAC with $^{15}O_2$, the recirculating water was estimated using the conventional modelling approach using

equation (7) (Iida *et al* 1993). Then, sets of two input functions for pure $^{15}O_2$ and $H_2^{15}O$ were obtained, which were denoted as true input functions (TIFs). Those two blood TACs for $H_2^{15}O$ and $^{15}O_2$ were added with a time lag of 180 s of the order of $H_2^{15}O$ and $^{15}O_2$ and reverse for the $H_2^{15}O$–$^{15}O_2$ and $^{15}O_2$–$H_2^{15}O$ protocols, respectively, and the CIFs were obtained. Note that two blood TACs without the correction for the physical decay of $^{15}O$ were used prior to combining, and the combined curve was corrected for the physical decay of $^{15}O$.

Methods (A) and (B) were applied to the CIFs to separate the $^{15}O_2$ and $H_2^{15}O$ contents. For method (A), the fitting period was selected from 80, 100, 120, 140 and 160 s to 180 s.

*2.2.3. Computation of functional values.* Values of CBF, OEF and $CMRO_2$ were calculated from tissue TAC ($C_i(t)$) and separated input functions for $H_2^{15}O$ ($F_w(t)$) and for $^{15}O_2$ ($F_o(t)$) using mathematical formulae, based on a single-tissue compartment model for water and oxygen (Mintun *et al* 1984). The formulae were designed to be applicable to data for tracer administration in either order $H_2^{15}O$–$^{15}O_2$ or $^{15}O_2$–$H_2^{15}O$. The total radioactivity in the tissue after $^{15}O_2$ and $H_2^{15}O$ administration can be expressed as,

$$C_i(t) = f \cdot F_w \otimes e^{\frac{-fA}{p}} + E \cdot f \cdot F_o \otimes e^{\frac{-fA}{p}} + V_B \cdot R_{Hct}(1 - F_v \cdot E)F_o(t) \tag{17}$$

where $f$ is CBF, $E$ is the OEF, $p$ is a blood/brain partition coefficient for water, $V_B$ is cerebral blood volume, $R_{Hct}$ is the small-to-large vessel haematocrit ratio and $F_v$ is the effective venous fraction. The first term on the right-hand side describes the amount of water entering the tissue. The second represents the amount of oxygen that enters the tissue and is immediately metabolized to water. The third expresses the radioactivity of $^{15}O_2$ in blood vessels. In the present study, we assumed that the radioactivity of $H_2^{15}O$ in the blood vessel term is negligibly small compared to the radioactivity in tissue according to the previous study (Iida *et al* 2000).

To calculate functional values using a look-up table procedure, equation (17) was integrated for the periods after $H_2^{15}O$ ($\int_w$: integrate for 90 s after rise up of $H_2^{15}O$ tissue TAC) and $^{15}O_2$ administration ($\int_o$: integrate for 180 s after rise up of $^{15}O_2$ tissue TAC) as

$$\int_w C_i(t)\,dt = \int_w (f \cdot F_w \otimes e^{\frac{-fA}{p}} + E \cdot f \cdot F_o \otimes e^{\frac{-fA}{p}} + V_B \cdot R_{Hct}(1 - F_v \cdot E)F_o(t))\,dt \tag{18}$$

$$\int_o C_i(t)\,dt = \int_o (f \cdot F_w \otimes e^{\frac{-fA}{p}} + E \cdot f \cdot F_o \otimes e^{\frac{-fA}{p}} + V_B \cdot R_{Hct}(1 - F_v \cdot E)F_o(t))\,dt. \tag{19}$$

Equation (19) can be rewritten as

$$E = \frac{\int_o (C_i(t)\,dt - f \cdot F_w \otimes e^{\frac{-fA}{p}} - V_B \cdot R_{Hct} \cdot F_o(t))\,dt}{\int_o (E \cdot f \cdot F_o \otimes e^{\frac{-fA}{p}} - V_B \cdot R_{Hct} \cdot F_v \cdot F_o(t))\,dt}. \tag{20}$$

Substituting equation (20) into (18), we obtain

$$\begin{aligned}\int_w C_i(t)\,dt = {} & \int_w (f \cdot F_w \otimes e^{\frac{-fA}{p}} + V_B \cdot R_{Hct} \cdot F_o(t))\,dt \\ & + \int_w (f \cdot F_o \otimes e^{\frac{-fA}{p}} - V_B \cdot R_{Hct} \cdot F_v \cdot F_o(t))\,dt \\ & \times \frac{\int_o (C_i(t)\,dt - f \cdot F_w \otimes e^{\frac{-fA}{p}} - V_B \cdot R_{Hct} \cdot F_o(t))\,dt}{\int_o (E \cdot f \cdot F_o \otimes e^{\frac{-fA}{p}} - V_B \cdot R_{Hct} \cdot F_v \cdot F_o(t))\,dt}.\end{aligned} \tag{21}$$

Using equation (21), $f$ can be estimated using a look-up table procedure based on the tissue TAC and separated input functions. Next, $E$ can be calculated using equation (20). $CMRO_2$ is

then calculated from the estimated $f$ and $E$, and the measured arterial oxygen content ($[O_2]_a$) as $CMRO_2 = 1.36 \cdot [O_2]_a \cdot E \cdot f$.

*2.2.4. Error analysis in the separation procedure.* The error in the separation of the input function by the proposed methods propagates into the quantitative values of CBF and $CMRO_2$. This error propagation was investigated by the simulation study.

Ten sets of TIFs for $H_2^{15}O$ and $^{15}O_2$ were used to generate tissue TACs using equation (17). Two sets of physiological conditions were simulated, namely the normal condition (CBF = 50 ml/100 g $min^{-1}$, OEF = 0.4, CBV = 0.04 ml $g^{-1}$, $p = 0.8$ ml $g^{-1}$, $F_v = 0.835$, and $R_{Hct} = 0.85$) (Hayashi *et al* 2003) and ischaemic condition (CBF = 20 ml/100 g $min^{-1}$, OEF = 0.7, CBV = 0.04 ml $g^{-1}$, $p = 0.8$ ml $g^{-1}$, $F_v = 0.835$ and $R_{Hct} = 0.85$).

The combined tissue TACs for both orders of the DARG protocol, i.e. $H_2^{15}O$–$^{15}O_2$ and $^{15}O_2$–$H_2^{15}O$ were created by adding generated tissue TACs of $H_2^{15}O$ and $^{15}O_2$ with a 3 min time lag.

The values of CBF and $CMRO_2$ were calculated according to the formulae described above (equations (20) and (21)) using separated input functions from the CIF and the combined tissue TACs. The errors in the form of biases and deviations in estimated CBF and $CMRO_2$ values were calculated by comparing them with the assumed CBF and $CMRO_2$ values. These errors were presented as percentage differences between the calculated and assumed values.

*2.2.5. Influence of dose of second tracer.* In the DARG protocol, if administration dose of the second tracer is relatively smaller than that of the first tracer, the portion of the residual radioactivity from the first tracer in the second blood TAC becomes larger. Contrarily, if administration dose of the second tracer is larger than that of the first tracer, contribution of residual radioactivity from the first tracer on the second blood TAC becomes smaller. Therefore, errors of the separation methods and consequently the errors in the values of CBF and $CMRO_2$ might depend on the administration dose of the second tracer with respect to that of the first tracer.

We investigated how the error size would change when the second dose, i.e. the amount of the second input function, changed. For this purpose, the height of the oxygen input function in CIF was changed so that the ratio of the AUC (area under curve) between the $H_2^{15}O$ and $^{15}O_2$ input functions was changed stepwise from half to two-fold. The error size in the CBF and $CMRO_2$ values was analysed in the same way as above using separation methods (A) and (B).

*2.2.6. Influence of noise in arterial TAC.* The size of the error in the values of CBF and $CMRO_2$ might also depend on the statistical fluctuation in the arterial TAC, and we investigated the change in error size in the CBF and $CMRO_2$ values when the statistical fluctuations of the arterial TAC changed. To investigate the error size, 1000 noisy arterial TACs (noisy CIF) were created by adding Gaussian noise to the CIFs. The noise was added every second in a form given by $n(t) = \alpha \cdot G(\sqrt{C(t)})$. Here, $C(t)$ and $n(t)$ denote the arterial TAC count in a second without decay and noise correction at time $t$, respectively, and $G(\sigma)$ is the Gaussian noise with the standard deviation $\sigma$. The noise level $\alpha$ was defined so that the coefficient of variance in the water arterial TAC at its peak was set to 1, 2, 4, 8, 16 and 32%. The noisy arterial TACs were separated by methods (A) and (B). The values of CBF and $CMRO_2$ were then calculated using these separated TACs, and the errors in the form of biases and deviations in those values were presented as percentage differences from the assumed values. In addition, noise was also added to TIFs, and CBF, OEF and $CMRO_2$ were calculated to investigate how the noise in the

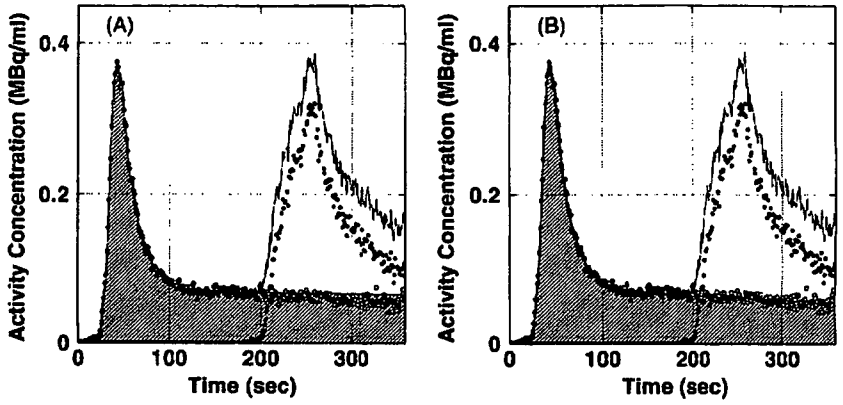


**Figure 2.** Estimated input function in the second phase (hatched region) from blood TAC (solid line) for DARG of $H_2^{15}O$–$^{15}O_2$. The blood TACs in which two components coexist were derived by combining two blood TACs of $^{15}O$-water (white circles) and $^{15}O$-oxygen (black circles) with a 180 s time lag. (A) Residual radioactivity of the first tracer was estimated by method (A) (fitting interval: 120 to 180 s). (B) Residual radioactivity of the first tracer was estimated by method (B).

arterial TAC without the separation procedure contributes to errors in the CBF, OEF and $CMRO_2$ values.

## 3. Results

Among ten normal subjects, the mean values of AUC for a period of 180 s for the arterial TAC were 80 ± 19 kBq $ml^{-1}$ and 55 ± 10 kBq $ml^{-1}$ for $H_2^{15}O$ and $^{15}O_2$, respectively. This result indicated that the values of AUC for $H_2^{15}O$ and $^{15}O_2$ had an ambiguity of approximately 20%, although all the subjects received the same amount of dose and processes for administration in the present PET study condition.

Figures 2 and 3 show examples of the separated input functions for the DARG protocols of $H_2^{15}O$–$^{15}O_2$ and $^{15}O_2$–$H_2^{15}O$ with the original and combined input functions using methods (A) and (B). It took about 40 s to separate the input function in method (B), and less than 1 s in method (A) (CPU: Intel® Pentium® D 3.2 GHz, memory: 1.0 GB, OS: Linux Fedora Core 4). For both methods and protocols, the estimated residual radioactivity in the second phase with respect to the first (hatched region) was almost identical to the true (original) input function (white circle).

For the linear method (A), the fitting interval from 120 to 180 s, where the slope of the input function became stable, provided the best fit for both the protocols, as shown in table 1. The table shows the fitting interval provided minimal bias and deviation in the difference of area under the curve between CIF and separated TAC for the residual tracer radioactivity in the second phase. When the start time of that interval was less than 120 s, the change in slope of the input function for the first tracer was large and the linear function could not reproduce the TAC of the residual radioactivity in the second phase. Further, when the time was greater, the amount of data was too inadequate to reproduce the TAC in the second phase.

Table 2 summarizes the error in the CBF and the $CMRO_2$ values due to the separation in input functions. The size of the bias and deviation in the CBF and the $CMRO_2$ values were within 4% for all separation procedures in both conditions.

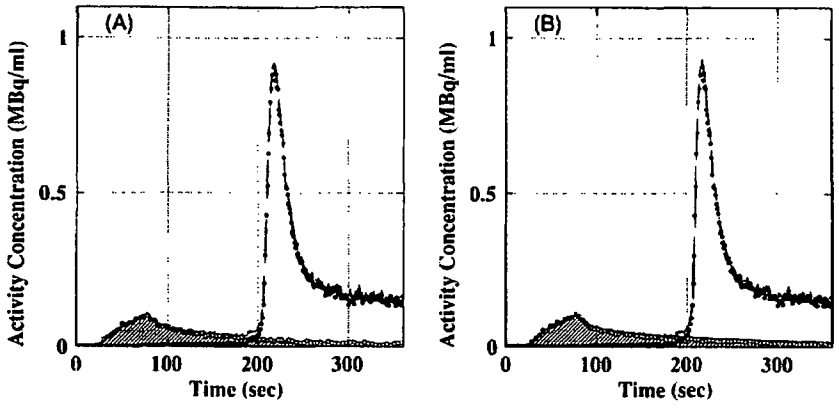


**Figure 3.** Estimated input function in the second phase (hatched region) from blood TAC (solid line) for DARG of $^{15}O_2$–$H_2^{15}O$. The blood TAC in which two components coexist was derived by combining two blood TACs of $^{15}O$-oxygen (black circles) and $^{15}O$-water (white circles) with a 180 s time lag. (A) Residual radioactivity of the first tracer was estimated by method (A) (fitting interval: 120 to 180 s) (B) Residual radioactivity of the first tracer was estimated by method (B).

**Table 1.** Bias and deviation in the difference of area under the curve between CIF and the estimated residual tracer radioactivity in the second phase by the linear method against the fitting interval ($n$ = 10). Bias and deviation are given in %.

| Fitting interval (s) | 60–180 | 80–180 | 100–180 | 120–180 | 140–180 | 160–180 |
|---|---|---|---|---|---|---|
| $H_2O$–$O_2$ protocol | 106.9 ± 37.8 | 46.7 ± 44.3 | 10.5 ± 20.8 | 0.5 ± 14.5 | −1.8 ± 17.2 | 25.4 ± 40.3 |
| $O_2$–$H_2O$ protocol | 9.1 ± 5.6 | 8.7 ± 7.2 | 7.2 ± 6.6 | 5.3 ± 4.5 | 5.6 ± 7.2 | 7.7 ± 15.6 |

**Table 2.** Bias and deviation in CBF and $CMRO_2$ propagated from the error in the separation of $^{15}O_2$ and $H_2^{15}O$ input function ($n$ = 10).

| | | Bias ± deviation (%) | | | |
|---|---|---|---|---|---|
| | | Normal condition | | Ischaemic condition | |
| Model function | Fitting interval (s) | CBF | $CMRO_2$ | CBF | $CMRO_2$ |
| $H_2^{15}O$–$^{15}O_2$ | | | | | |
| (A) | 120–180 | - | −1.9 ± 4.2 | - | −2.2 ± 3.5 |
| (B) | 0–360 | - | 0.4 ± 1.6 | - | 0.3 ± 1.9 |
| $^{15}O_2$–$H_2^{15}O$ | | | | | |
| (A) | 120–180 | −2.1 ± 1.2 | 1.3 ± 0.6 | −1.7 ± 1.1 | 1.7 ± 0.6 |
| (B) | 0–360 | −0.3 ± 1.4 | 0.2 ± 0.5 | −0.2 ± 1.7 | 0.2 ± 0.1 |

Normal condition: CBF = 50 ml $min^{-1}$/100 g, OEF = 0.4; ischaemic condition: CBF = 20 ml $min^{-1}$/100 g, OEF = 0.7.

The bias and deviation in the value of CBF for $^{15}O_2$–$H_2^{15}O$ and $CMRO_2$ for both $H_2^{15}O$–$^{15}O_2$ and $^{15}O_2$–$H_2^{15}O$ are shown as functions of the ratio of AUC between the first and second input functions in figure 4. The size of the bias and deviation increased with the decrease in the second tracer dose and was suppressed since the second dose was increased in both methods (A) and (B). The size of the bias in the CBF by the $^{15}O_2$–$H_2^{15}O$ protocol and the $CMRO_2$ by the $H_2^{15}O$–$^{15}O_2$ protocol was 2% at most and was almost the same in the range of the AUC ratio from half to two-fold. The size of the bias in $CMRO_2$ by the $^{15}O_2$–$H_2^{15}O$ protocol was

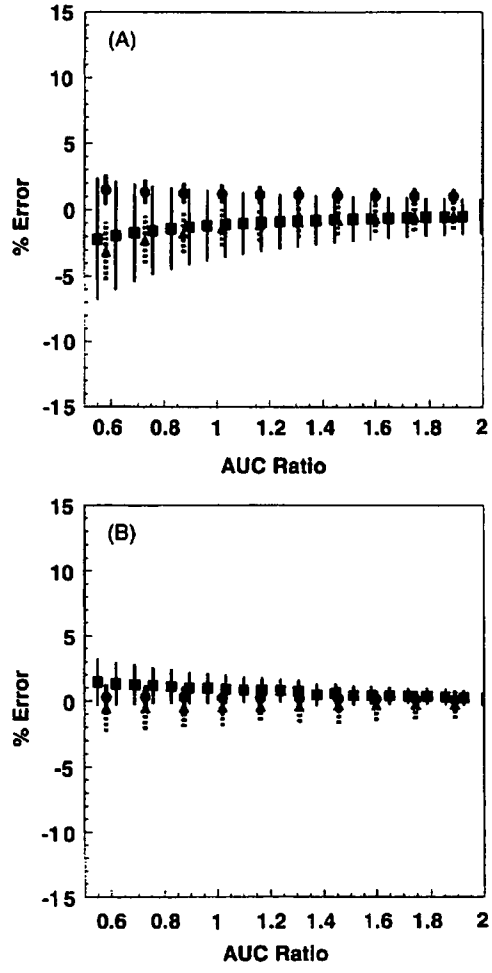


**Figure 4.** Error in CBF and $CMRO_2$ as a function of the dose ratio between the first to second tracer using separated input functions in method (A) (top) and (B) (bottom). The sizes of the bias in the values of CBF for $^{15}O_2$–$H_2^{15}O$ (circles) and $CMRO_2$ for $H_2^{15}O$–$^{15}O_2$ (squares) and $CMRO_2$ for $^{15}O_2$–$H_2^{15}O$ (triangles) are plotted and that of the deviation is expressed as the length of the bar.

almost negligible, and it was smaller than 0.5% in the same range of the AUC ratio. The size of the deviation for the CBF in the $^{15}O_2$–$H_2^{15}O$ protocol was less than 0.5%, and the sizes of the deviation for $CMRO_2$ in the $^{15}O_2$–$H_2^{15}O$ protocol and the $H_2^{15}O$–$^{15}O_2$ protocol were less than 3% and 4%, respectively.

The size of the bias and the deviation in the CBF, OEF and $CMRO_2$ values, due to the noise in the arterial TAC are shown in figure 5. The size of the bias for the separation method (B) (denoted by triangles) in those values was less than 5% when the noise level was less than 10%, and it was almost identical to that estimated using noisy TIF (denoted by circles). The bias by method (A) (denoted by squares) was larger than that by method (B). For the deviation with respect to the noise TIF, the size of the error in the CBF, OEF and $CMRO_2$ values was almost identical for both methods (A) and (B).

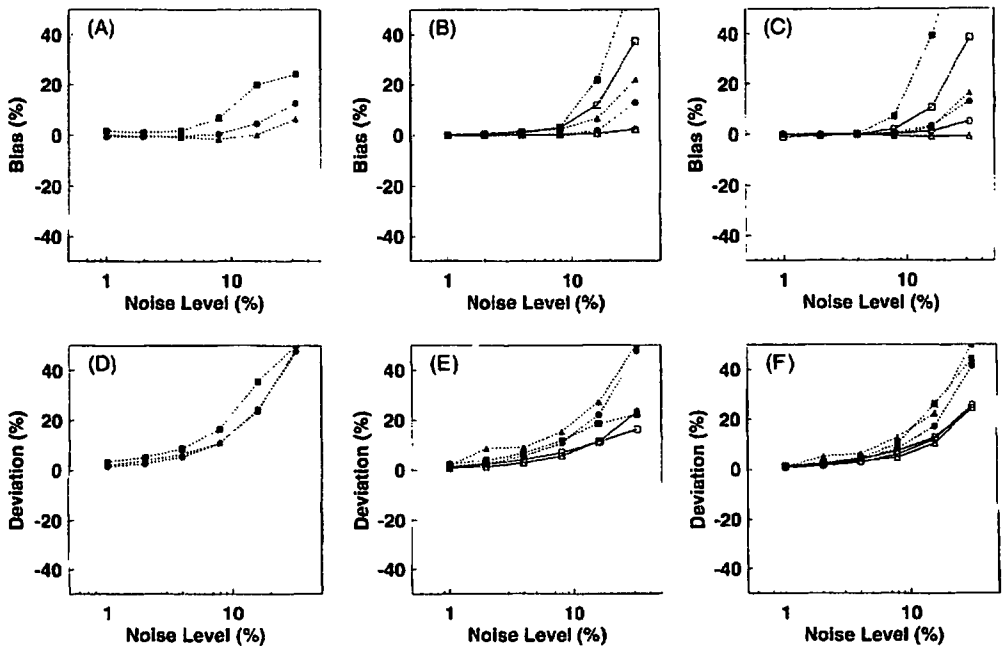


**Figure 5.** Bias (upper) and deviation (lower) against noise level in CBF (left), OEF (centre) and $CMRO_2$ (right) propagated from the noise on arterial TAC. The CBF, OEF and $CMRO_2$ were calculated with a noisy input function (circles) and separated input functions from the noisy arterial TAC by methods (A) (squares) and (B) (triangles), respectively. The orders of tracers $H_2^{15}O$–$^{15}O_2$ and $^{15}O_2$–$H_2^{15}O$ are indicated by white and black symbols, respectively.

## 4. Discussion and conclusion

We developed the separation methods of dual tracer coexistent blood TAC for the DARG protocol to avoid frequent blood sampling to calculate the quantitative CBF, OEF and $CMRO_2$ images. The present results showed that the values in CBF and $CMRO_2$ using input functions separated by the present method were reasonably accurate, i.e., the bias and deviation in CBF, OEF and $CMRO_2$ values were within 4%. When the dose of the second tracer was changed, the bias and deviation in CBF and $CMRO_2$ also changed; however, the sizes were within 5% when the ratio between AUCs in the first and second input functions was from half to two-fold. Further, the bias and deviation in the CBF and $CMRO_2$ values due to noise in the arterial TAC was less than 5% and was not severely enhanced against those from the noisy TIF.

The present results showed that the model-based function method (B) provided a more accurate value for CBF and/or $CMRO_2$ in both the $H_2^{15}O$–$^{15}O_2$ and the $^{15}O_2$–$H_2^{15}O$ protocols. The reason of the better performance of method (B) was the use of the entire period of data, although the expression of the model function was complex and the calculation took a longer time.

On the other hand, in the linear method (A), the arterial TAC was fitted with the linear function during a period of 120 to 180 s in the first phase, i.e. during the period after the shape of the first input function in the stable state, and the residual radioactivity was then estimated by extrapolating that function in the second phase. The bias and deviation in CBF and $CMRO_2$, calculated using separated input functions by method (A), were still within 4% and might be

acceptable for calculation. Thus, the present findings suggest that the dual tracer coexistent blood TAC can be separated by the linear function within a 4% accuracy. The advantages of method (A) over method (B) are easier implementation and faster computation. The linear regression program for the method (A) is readily available. On the other hand, for method (B), a computing framework for nonlinear fitting is required. We used the PAW environment for this purpose and fitting results might be different if another framework is employed. The benefit of faster computation could be minimized if a faster processor is used.

For the $^{15}O_2$–$H_2^{15}O$ protocol, the value of $CMRO_2$ was affected by the error in the separated input function, although the input function for calculating $CMRO_2$ was extracted in the first phase. This is because the $CMRO_2$ value was calculated not only from the input function and tissue TAC in the $^{15}O_2$ phase but also from the value of CBF that was estimated in the second phase and was affected by the separation error. However, the size of the error in $CMRO_2$ in $^{15}O_2$–$H_2^{15}O$ was less than 0.5% which is negligibly small. Further, the value for CBF in the $H_2^{15}O$–$^{15}O_2$ was unaffected by the error in separation, i.e., the CBF value was calculated exclusively in the first phase.

When the AUCs in the input function were almost the same between the first and second phases, the size of the bias in the value of CBF and $CMRO_2$ determined from the input function for the second phase tracer, i.e. CBF value for the $^{15}O_2$–$H_2^{15}O$ and $CMRO_2$ value for $H_2^{15}O$–$^{15}O_2$, was in the same range and was acceptable (figure 4). Moreover, the size of the bias was within a reasonable range when the ratio of the AUC between the first and second changed from half to two-fold. Practically, the present PET study on normal subjects showed that the fluctuation of the AUC of the input function was 20% when the tracer was administrated by the same procedure. This suggests that the degree of error due to the change in the ratio of the AUC of the input functions across subjects between the first and second phases could be within an acceptable range; further, the degree of error with regard to other error factors, such as delay or dispersion in input function was the same (Kudomi *et al* 2005).

Many PET scanners recently available are combined with CT scanners, and the patients reside deep inside the scanner housing during PET scanning. In this case, the length of the catheter tube must be long, which results in longer delay time and worse statistics in measured blood TAC. The size of errors as bias and deviation in CBF, OEF and $CMRO_2$ due to noise in the arterial blood TAC was less than 5% when the noise level was less than 10%. The 10% noise level corresponds to 100 cps in the measured water arterial TAC at its peak. Most devices monitoring arterial TAC can provide this level of statistics in practical examination for CBF, OEF and $CMRO_2$ evaluation for both 3SARG and DARG. Moreover, the degree of error in these values was not enhanced in comparison to that from noisy TIF. Thus, the separation procedure due to noise on the arterial TAC might not deteriorate the quantitative accuracy in CBF, OEF and $CMRO_2$.

The image quality in CBF and $CMRO_2$ by the DARG approach is influenced by the interval, relative dose, and order of the two administered tracers. Since the dose of the second tracer is less, a relatively larger amount of residual radioactivity from the first tracer remains during the image acquisition for the second tracer, and it results in the degradation of the quality of the image obtained during the second phase of the procedure. Thus, the dose of the second tracer should be as high as possible for the DARG approach in terms of the separation of the input function. However, when the dose of the second tracer is too high, the amount of random photons and dead time in the PET data would increase and the quantitative accuracy might be degraded. Further, the radiation dose increases for patients. These matters suggest that the amount and ratio of the tracer dose assumed in the present study might be appropriate for the DARG PET measurement.